Supplementary Information

From 0D $Cs_3Bi_2I_9$ to 2D $Cs_3Bi_2I_6Cl_3$: Dimensional Expansion Induces Direct Bandgap but Enhances Electron-Phonon Coupling

Kyle M. McCall,[†,‡] Constantinos C. Stoumpos,[†] Oleg Y. Kontsevoi,[§] Grant C. B. Alexander,[†] Bruce W. Wessels,[‡] Mercouri G. Kanatzidis*[,†]

[†]Department of Chemistry, [‡]Department of Materials Science and Engineering, [§]Department of Physics and Astronomy, Northwestern University, Evanston, Illinois 60208, United States

Table S1. Crystal data and structure refinement for $Cs_3Bi_2I_6Cl_3$ at 293(2) K.

Empirical formula	$Cs_3Bi_2I_6Cl_3$
Formula weight	1684.44
Temperature	293(2) K
Wavelength	0.71073 Å
Crystal system	Trigonal
Space group	*P*-3*m*1
Unit cell dimensions	a = 8.2432(17) Å, α = 90° b = 8.2432(17) Å, β = 90° c = 10.021(2) Å, γ = 120°
Volume	589.7(3) $Å^3$
Z	1
Density (calculated)	4.745 g/cm^3
Absorption coefficient	27.642 mm^{-1}
F(000)	700
Crystal size	0.305 x 0.029 x 0.025 mm^3
θ range for data collection	2.032 to 30.035°
Index ranges	-10<=h<=11, -11<=k<=11, -10<=l<=14
Reflections collected	5768
Independent reflections	696 [R_{int} = 0.0315]
Completeness to θ = 25.242°	100%
Refinement method	Full-matrix least-squares on F^2
Data / restraints / parameters	693 / 0 / 19
Goodness-of-fit	1.160
Final R indices [I > 2σ(I)]	R_{obs} = 0.0426, wR_{obs} = 0.1206
R indices [all data]	R_{all} = 0.0459, wR_{all} = 0.1242
Largest diff. peak and hole	2.916 and -2.641 $e \cdot Å^{-3}$

$R = \Sigma||F_o|-|F_c|| / \Sigma|F_o|$, $wR = \{\Sigma[w(|F_o|^2 - |F_c|^2)^2] / \Sigma[w(|F_o|^4)]\}^{1/2}$ and
$w=1/[\sigma^2(Fo^2)+(0.0631P)^2+7.4600P]$ where $P=(Fo^2+2Fc^2)/3$

Table S2. Atomic coordinates ($x10^4$) and equivalent isotropic displacement parameters ($Å^2x10^3$) for $Cs_3Bi_2I_6Cl_3$ at 293(2) K with estimated standard deviations in parentheses.

Label	x	y	z	Occupancy	U_{eq}*
Cs(1)	3333	6667	3107(2)	1	66(1)
Bi(2)	3333	6667	8301(1)	1	29(1)
Cs(2)	0	0	0	1	79(1)
I(1)	1647(1)	3294(2)	6681(1)	1	62(1)
Cl(1)	5000	5000	10000	1	64(2)

*U_{eq} is defined as one third of the trace of the orthogonalized U_{ij} tensor.

Table S3. Anisotropic displacement parameters ($Å^2x10^3$) for $Cs_3Bi_2I_6Cl_3$ at 293(2) K with estimated standard deviations in parentheses.

Label	U_{11}	U_{22}	U_{33}	U_{12}	U_{13}	U_{23}
Cs(1)	59(1)	59(1)	79(2)	30(1)	0	0
Bi(2)	29(1)	29(1)	29(1)	15(1)	0	0
Cs(2)	96(2)	96(2)	44(2)	48(1)	0	0
I(1)	66(1)	45(1)	68(1)	22(1)	-11(1)	-22(1)
Cl(1)	87(4)	87(4)	49(3)	67(4)	-14(2)	14(2)

The anisotropic displacement factor exponent takes the form: $-2\pi^2[h^2a^{*2}U_{11} + ... + 2hka^*b^*U_{12}]$.

Table S4. Selected bond lengths [Å] for $Cs_3Bi_2I_6Cl_3$ at 298(2) K with estimated standard deviations in parentheses.

Label	Distances
Bi(2)-I(1)	2.9032(10)
Bi(2)-Cl(1)	2.9258(4)

Table S5. Selected bond angles [°] for $Cs_3Bi_2I_6Cl_3$ at 298(2) K with estimated standard deviations in parentheses.

Label	Angles
I(1)'-Bi(2)-I(1)	91.80(4)
I(1)'-Bi(2)-Cl(1)	178.40(3)
I(1)-Bi(2)-Cl(1)	89.319(19)
Cl(1)'-Bi(2)-Cl(1)	89.543(19)

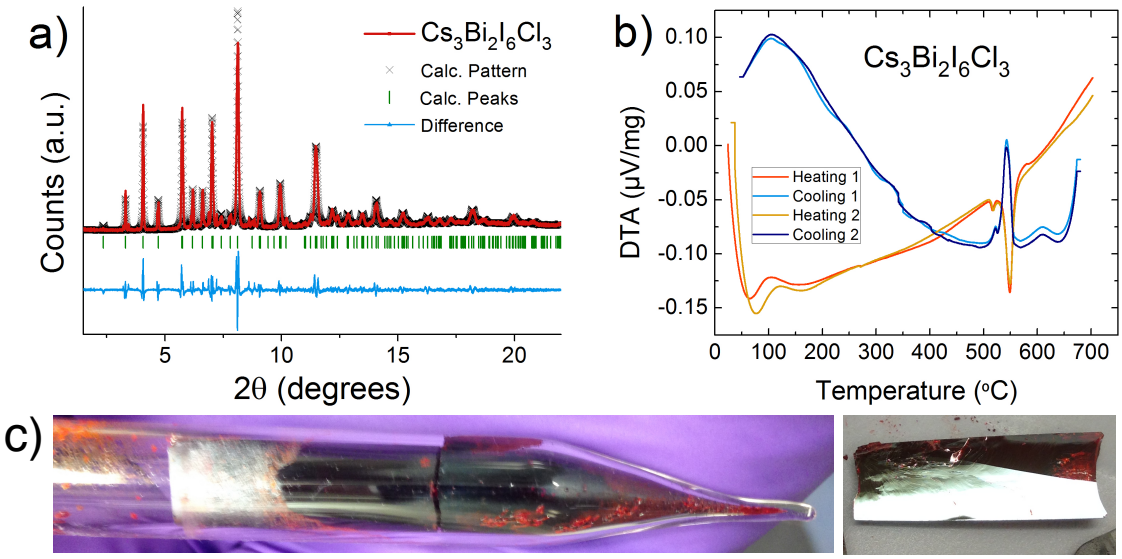

Figure S1. (a) Synchrotron PXRD of $Cs_3Bi_2I_6Cl_3$ (red line, pattern matched by the fit line indicated by black crosses, with green bars denoting reflection peaks). (b) Differential thermal analysis (DTA) of $Cs_3Bi_2I_6Cl_3$, cycled twice to show reproducibility. We observe two melting events on heating at 517 ºC and 548 ºC with corresponding crystallization events on cooling. The broad bumps at the beginning of each cycle (at 50-120 ºC on heating and 580-650 ºC on cooling) are background resulting from instrument responses to the changing flow of gas around the sample. (c) Bridgman-grown ingot of $Cs_3Bi_2I_6Cl_3$ and cleaved single crystal

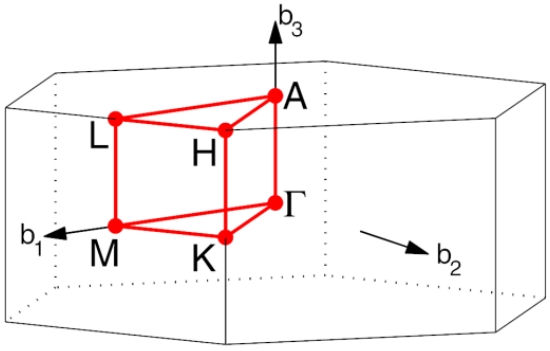

Figure S2. The hexagonal Brillouin zone used for DFT calculations of the electronic band structure of $Cs_3Bi_2I_6Cl_3$.

Estimating Effective Masses with DFT

Using the calculated band structure shown in Figure 3, the charge carrier effective masses were estimated by solving for the eigenvalues of the effective mass tensor at the conduction band minimum and valence band maximum. The calculated effective masses share the anisotropy of the 2D bilayer structure, with reasonable in-plane effective masses of 0.44 m_e for electrons and 0.48 m_e for holes, while the out-of-plane direction has less dispersive bands with larger effective masses of 0.63 m_e and 1.8 m_e for electrons and holes, respectively. This is in contrast with the electronic structure of the 2D $A_3M_2I_9$ compounds, which do not reflect the structural anisotropy of the 2D structure, instead offering reasonable effective masses in the out-of-plane direction and two different, larger effective masses in the in-plane directions.[1] This distinction is likely because the effective mass behavior in $Cs_3Bi_2I_6Cl_3$ reflects not just the structural anisotropy of the 2D structure, but more importantly the anisotropy of I and Cl stacking. According to the DOS picture of the CB states shown in Fig. 3(b), the electron transport is facilitated by strongly hybridized I*p*-Bi*p* antibonding orbitals with good orbital overlap, and such transport occurs exclusively through terminal I sites. However, these overlaps are disrupted in the out-of-plane direction due to a necessary involvement of Cl atoms, which have less overlap with Bi due to smaller radius,

resulting in the increased out-of-plane electron effective masses. The effect is even more dramatic for hole transport, which is carried out in-plane mostly through I*p*-Bi*s* bonding orbitals. For the out-of-plane direction hole transport is facilitated by a much weaker Cl*p*-Bi*s* orbital overlap, which results in a significant increase of the hole effective mass. In order to test the hypothesis that the anisotropy of the effective masses is due to Cl, we performed DFT calculation of the band structure and effective masses for a hypothetical compound $Cs_3Bi_2I_6I_3$ in which Cl atoms were replaced by I atoms, but the 2D crystal structure of $Cs_3Bi_2I_6Cl_3$ was kept unchanged. This hypothetical compound shows similar features of the band structure as $Cs_3Bi_2I_6Cl_3$, has a direct band gap of a similar width, but has a dramatically different behavior of effective masses. In-plane effective masses are 0.24 m_e for electrons and 0.58 m_e for holes, while out-of-plane effective masses are 0.39 m_e and 0.41 m_e for electrons and holes, respectively. The 1.6-1.8 times decreased electron effective masses reflect easier transport facilitated exclusively by I*p*-Bi*p* orbital overlap without disruption from Cl. The most dramatic effect is for out-of-plane hole transport, where hole effective masses were decreased fourfold, from 1.85 to 0.41, by replacing Cl*p*-Bi*s* orbital overlaps with I*p*-Bi*s* overlaps. Thus, Cl in $Cs_3Bi_2I_6Cl_3$ not only stabilizes its 2D layered structure, but also increases anisotropy of electronic properties of this compound.

$Cs_3Bi_2I_6Cl_3$ Photoluminescence Results and Fitting Details

The photoluminescence of $Cs_3Bi_2I_6Cl_3$ at 13 K under 405 nm excitation shows a broad band which is skewed to low energy (Figure 4, Figure S3a) in the same manner as the emission of $Rb_3Sb_2I_9$ and $Cs_3Sb_2I_9$.[2] A large number of Gaussian peaks is required to model this emission, so instead an exponentially modified Gaussian peak is used to account for the skewed emission:[3]

$$I(E) = \frac{A}{\mu}\exp\left[\frac{1}{2}\left(\frac{\omega}{\mu}\right)^2 - \frac{E - E_{max}}{\mu}\right]\int_{-\infty}^{z}\frac{1}{\sqrt{2\pi}}e^{-\frac{x^2}{2}}dx \text{ , where } z = \frac{E - E_{max}}{\omega} - \frac{\omega}{\mu} \text{ and} \quad (S1)$$

ω is the Gaussian peak width, E and E_{max} are the photon and peak energies, respectively, and A is the emission amplitude. The modification/skewness factor μ determines the direction and amplitude of the asymmetry in the line shape.

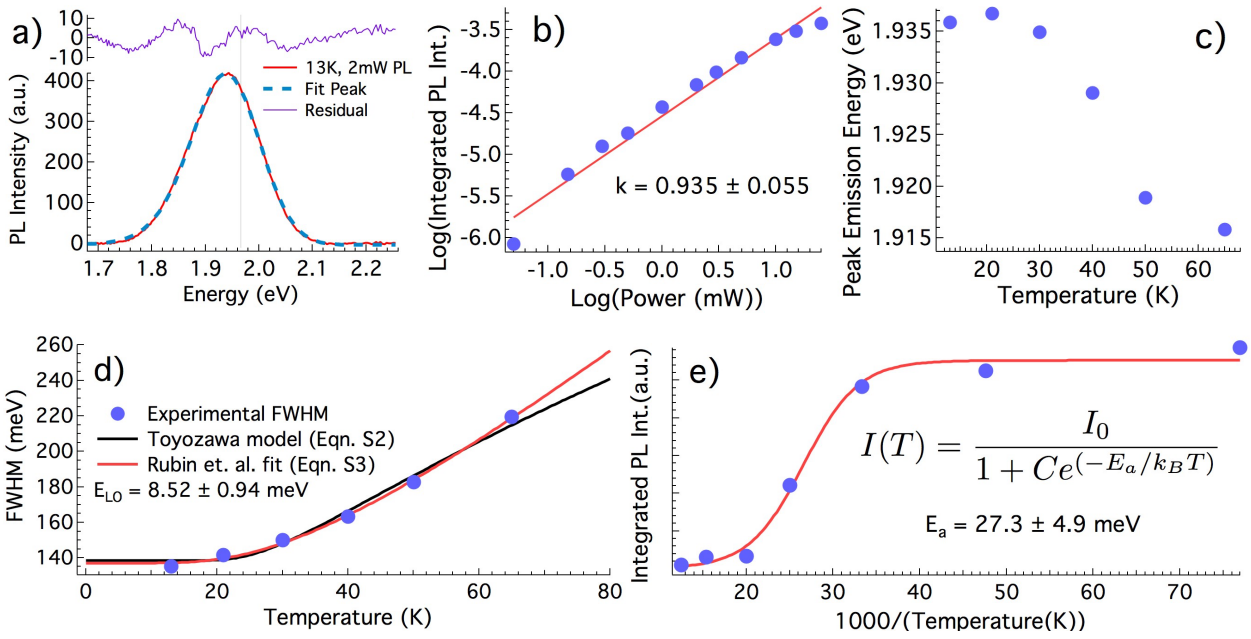

Figure S3. $Cs_3Bi_2I_6Cl_3$ photoluminescence: (a) PL experimental data (orange trace) at 2mW, 13 K fit by an exponentially modified Gaussian peak according to Eqn. S1 (blue dashed line), with the residual plotted above (purple). (b) log(integrated PL intensity) vs. log(laser power) showing the power-law dependence with the power law coefficient k extracted by a linear fit. (c) PL peak emission energy versus temperature showing a redshift with rising temperature. (d) Full-width at half-maximum vs. temperature, with least squared fits corresponding to phonon broadening models following Eqns. S2 and S3 portrayed by solid black and red lines, respectively. (e) Arrhenius plot of integrated PL intensity vs. 1000/temperature, with the solid red line corresponding to a least squared fit of the thermal quenching model described by Eqn. S4.

This expression has been previously used in analysis of the skewed photoluminescence peak of Ge[4] as well as the $A_3M_2I_9$ defect perovskites (A = Cs, Rb; M = Bi, Sb),[2] and describes the shape of the emission quite well (Figure S3a). This skewed peak shape is characteristic of phonon-assisted recombination of self-trapped excitons, which is the convolution of multiple overlapping peaks separated by the phonon energy E_{ph}.[2, 5] These peaks are located at an energy $E_n = E_g - nE_{ph}$ with an intensity which follows the Poisson distribution $I(n) = \frac{e^{-S}S^n}{n!}$, where n is the number of phonons associated with the transition and S is the Huang-Rhys parameter that governs the electron-phonon coupling.[5] The low-energy tail results from nonzero probabilities of high n number transitions, while the lower n numbered transitions must cease at $n = 0$ and thus have a sharper drop off.

Beyond this resemblance in shape, the intensity- and temperature-dependent emission characteristics also match those previously reported in the $A_3M_2I_9$ defect perovskites. Varying the excitation intensity of the 405 nm laser over the wide range of 0.05 mW to 25 mW does not shift the PL peak maximum nor alter the lineshape (Figure 4b), indicating that a single mechanism dominates the emission. The dependence of the photoluminescence intensity I on the excitation intensity L is governed by the power law $I \sim L^k$.[6] In this case the derived power law coefficient k is 0.935 ± 0.055 (Figure S3b), slightly higher than that of $Cs_3Sb_2I_9$ (0.89).[2]

To determine the temperature-dependent quenching behavior of the $Cs_3Bi_2I_6Cl_3$ emission, PL spectra were measured at 3 mW from 13 K until the emission quenched at ~80 K (Figure 4a). This is accompanied by a redshift in the PL peak maximum from 1.94 eV to 1.92 eV as temperature increases (Figure S3c). The width of the peak, as defined by the full-width at half maximum (FWHM), shows significant phonon broadening with increasing temperature, from 137.6 meV at 13 K to 233 meV at 65 K. The phonon broadening of the FWHM can be modeled

in two ways, following the approaches of Toyozawa[7] or of Rudin.[8]

The theory of Toyozawa models the emission broadening resulting from electron-phonon interactions with a configuration coordinate model where the FWHM, denoted *w(T)*, depends on the average phonon energy:[9]

$$w(T) = 2.36\sqrt{S} * E_{ph}\left[\coth\left(\frac{E_{ph}}{2k_BT}\right)\right]^{1/2} \quad (S2)$$

Here k_B is the Boltzmann constant, and again *S* is the Huang-Rhys electron-phonon coupling parameter and E_{ph} is the effective phonon energy. A least-squares fit of Equation S2 to the experimental data produces a good fit (black line, Figure S3d) with E_{ph} = 4.0 ± 0.4 meV, though the value derived for the Huang-Rhys coupling *S* is extremely high (212 ± 12). For reference, the $A_3M_2I_9$ compounds had *S* values in the range of 21.2 to 79.5,[2] and values above 100 are primarily found among the alkali halide salts, such as 120 for LiI.[10] However, a recent report finds a simulated value of 188 in the double perovskite $Cs_2NaInCl_6$,[11] indicating that such a strong electron-phonon coupling is not unreasonable. Indeed, we expect that moving from the relatively soft I atom to the ionic Cl should increase the polar nature of $Cs_3Bi_2I_6Cl_3$, thereby enhancing the electron-phonon coupling relative to the parent $A_3M_2I_9$ defect perovskites.

Following the approach of Wright *et al.*,[12], we can also use the model developed by Rudin *et al.* to describe the PL linewidth *Γ(T)* as the sum of four components:[8]

$$\Gamma(T) = \Gamma_0 + \Gamma_{ac} + \Gamma_{LO} + \Gamma_{imp} = \Gamma_0 + \gamma_{ac}T + \gamma_{LO}\left(e^{-E_{LO}/k_BT} - 1\right)^{-1} + \gamma_{imp}e^{-E_{imp}/k_BT} \quad (S3)$$

Here Γ_0 is a temperature independent term which arises from disorder, Γ_{ac} is due to acoustic phonon scattering, Γ_{LO} is due to Fröhlich scattering of longitudinal optical (LO) phonons, and the final term Γ_{imp} describes the contribution of ionized impurities.[8] As was found by Wright et al., the linear shape of the acoustic phonon term and the asymptotic approach of the impurity term do not match the behavior of the experimental FHWM data, and both coupling constants γ_{ac} and γ_{imp}

approach zero during fitting.[12] Thus, the dominant contribution is that of the optical phonons, and a least-squared fit of the experimental data to Equation S3 considering only the terms Γ_0 and Γ_{LO} produces an excellent fit (solid red line, Figure S3d) with Γ_0 = 137.1 ± 1.8 meV, γ_{LO} = 291.8 ± 61.9 meV, and the optical phonon energy is E_{LO} = 8.52 ± 0.94 meV. These values are reasonable and the LO phonon energy of 8.52 meV is in good agreement with the broad band of optical phonon modes observed in the Raman spectra near 66 cm^{-1} (8.2 meV). Similar agreement was observed in the $A_3M_2I_9$ defect perovskites,[2], and highlights the phonon-assisted nature of the radiative transition. Additionally, the high value of the LO coupling constant γ_{LO} (291.8 meV) in comparison to that of the 3D hybrid perovskites (40 – 61 meV) demonstrates the greater strength of the electron-phonon coupling in the lower-dimensional $Cs_3Bi_2I_6Cl_3$.[12] Altogether, these characteristics support the assignment of the PL to the phonon-assisted recombination of self-trapped excitons.

Finally, the thermal quenching behavior can be quantified by modeling the PL quenching as the activation of a competing nonradiative recombination process with activation energy E_a:[13]

$$I(T) = \frac{I_0}{1 + C\, e^{-\frac{E_a}{k_B T}}}, \qquad (S4)$$

where C and I_0 are constants. Fitting the Arrhenius plot of PL intensity versus inverse temperature with Equation S4 produces excellent agreement (red line, Figure S3e), and the derived activation energy is 27.3 ± 4.9 meV. This low activation energy explains the rapid quenching of the PL as temperature increases, and is consistent with the absence of PL at room temperature.

$Rb_3Bi_2I_6Cl_3$ Characterization

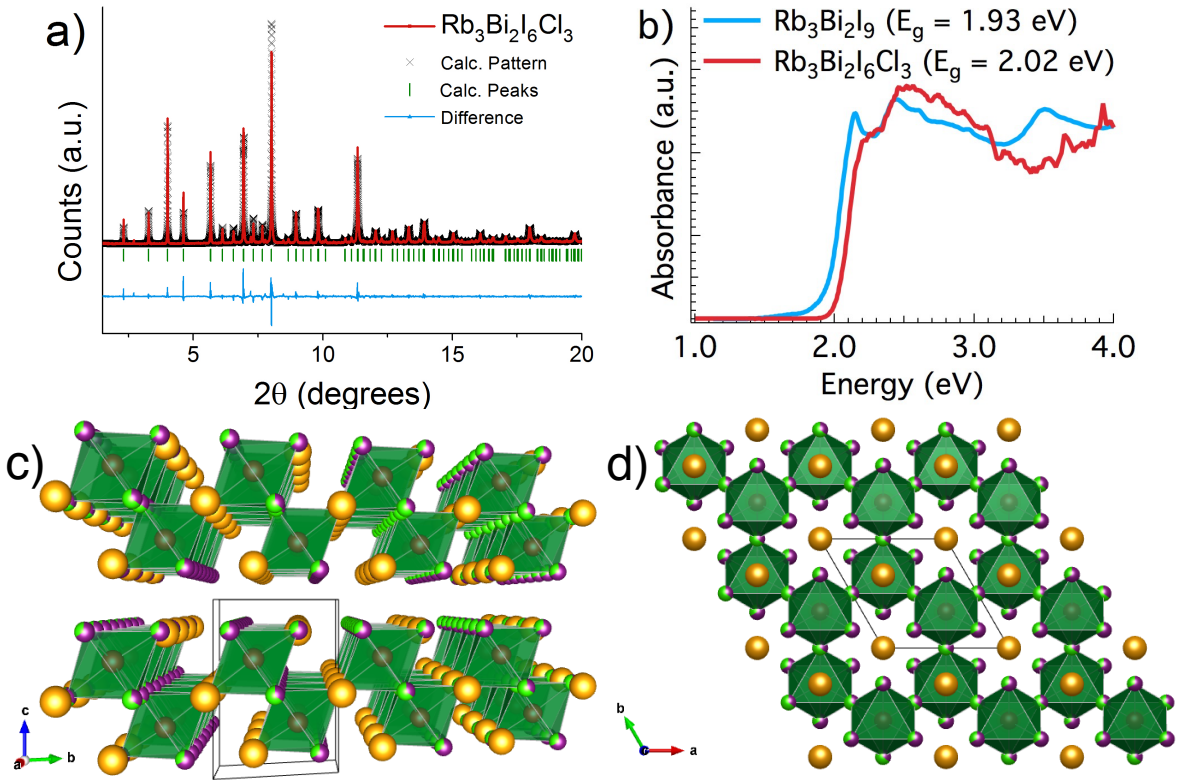

Figure S4. (a) Synchrotron PXRD of $Rb_3Bi_2I_6Cl_3$ (red line, fit line marked by black crosses, green bars denote peak positions). (b) UV-Vis reflectance of $Rb_3Bi_2I_6Cl_3$ and $Rb_3Bi_2I_9$. View of solved $Rb_3Bi_2I_5Cl_4$ crystal structure viewed down the (c) a-axis and (d) c-axis.

As another test of the effects of replacing the bridging I atoms with smaller Cl atoms, we tested the 2D monoclinic (space group $P2_1/n$) $Rb_3Bi_2I_9$ system, targeting the compound $Rb_3Bi_2I_6Cl_3$ in an attempt to restore the trigonal symmetry of the prototypical 2D defect perovskite. The 2D bilayer structure of $Rb_3Bi_2I_9$ is distorted due to the size imbalance of the Bi and Rb atoms, which are larger and smaller than the Sb and Cs counterparts, respectively. Addition of Cl atoms in the bridging site may relax the structure and permit an increase in symmetry, as it gives the structure flexibility to modify the bond lengths in order to maintain a comfortable coordination environment for the Rb atoms. Direct synthesis of RbCl and BiI_3 successfully produces a new, phase-pure trigonal structure (*P*-3*m*1, Figure S4a) with a band gap of 2.02 eV, slightly higher than the 1.93 eV gap of $Rb_3Bi_2I_9$ (Figure S4b). However, halide

segregation is incomplete in this system, as several crystal structure solutions produce a range of values for I and Cl occupancy (Figure S4c and S4d). As expected, the bridging site prefers the Cl atom (65 % Cl, 35 % I occupancy) while the majority of terminal sites are filled by I atoms (66 % I, 34% Cl occupancy), however they are not distinctly separate sites as in $Cs_3Bi_2I_6Cl_3$. This site mixing may be a factor in the relatively poor crystallinity of the as-grown crystals obtained via both solid-state synthesis as well as Bridgman growth, as phase separation may be occurring in the melt. Such segregation and imperfections are likely responsible for the high goodness of fit, as there are many extraneous peaks in the data collection, especially at high angles. The crystal structure obtained here adds up to a formula of $Rb_3Bi_2I_5Cl_4$, which is a Cl-rich composition with respect to the starting stoichiometry and implying that elsewhere in the melt exists an I-rich phase. Nevertheless, the uneven distribution of Cl and I does not reach the extent required to return to monoclinic symmetry of the parent $Rb_3Bi_2I_9$, as the material is phase-pure with trigonal symmetry and all monoclinic reflections are absent, even as measured by the high-resolution synchrotron at beamline 11-BM-B of the Advanced Photon Source (at Argonne National Laboratory).

Table S6. Crystal data and structure refinement for $Rb_3Bi_2I_5Cl_4$ at 293 K.

Empirical formula	$Rb_3Bi_2I_5Cl_4$
Formula weight	1451.3
Temperature	293 K
Wavelength	0.71073 Å
Crystal system	trigonal
Space group	P -3 m 1
Unit cell dimensions	a = 8.3673(9) Å, α = 90° b = 8.3673(9) Å, β = 90° c = 10.2506(13) Å, γ = 120°
Volume	621.51(12) $Å^3$
Z	1
Density (calculated)	3.8776 g/cm^3
Absorption coefficient	26.598 mm^{-1}
F(000)	608
Crystal size	0.26 x 0.19 x 0.11 mm^3
θ range for data collection	3.44 to 29.21°
Index ranges	-10<=h<=11, -11<=k<=4, -14<=l<=14
Reflections collected	2901
Independent reflections	457 [R_{int} = 0.1077]
Completeness to θ = 29.2°	98%
Refinement method	Full-matrix least-squares on F^2
Data / restraints / parameters	457 / 0 / 21
Goodness-of-fit	6.21
Final R indices [I>2σ(I)]	R_{obs} = 0.0750, wR_{obs} = 0.1803
R indices [all data]	R_{all} = 0.0774, wR_{all} = 0.1804
Largest diff. peak and hole	6.65 and -2.98 e·$Å^{-3}$

$R = \Sigma||F_o|-|F_c|| / \Sigma|F_o|$, $wR = \{\Sigma[w(|F_o|^2 - |F_c|^2)^2] / \Sigma[w(|F_o|^4)]\}^{1/2}$ and $w=1/(\sigma^2(I)+0.0004I^2)$

Table S7. Atomic coordinates ($x10^4$) and equivalent isotropic displacement parameters ($Å^2x10^3$) for $Rb_3Bi_2I_5Cl_4$ at 293 K with estimated standard deviations in parentheses.

Label	x	y	z	Occupancy	U_{eq}*
Bi	3333.33	6666.67	3176(2)	1	34(1)
Rb(1)	0	0	5000	1	51(2)
Rb(2)	6666.67	3333.33	1801(5)	1	46(2)
I(1)	1645(2)	3290(4)	1641(3)	0.66(2)	53(2)
Cl(1)	1645(2)	3290(4)	1641(3)	0.34(2)	53(2)
I(2)	5000	0	5000	0.35(3)	75(3)
Cl(2)	5000	0	5000	0.65(3)	75(3)

*U_{eq} is defined as one third of the trace of the orthogonalized U_{ij} tensor.

Table S8. Anisotropic displacement parameters ($Å^2x10^3$) for $Rb_3Bi_2I_5Cl_4$ at 293 K with estimated standard deviations in parentheses.

Label	U_{11}	U_{22}	U_{33}	U_{12}	U_{13}	U_{23}
Bi	32(1)	32(1)	38(1)	16(1)	0	0
Rb(1)	56(3)	56(3)	43(3)	28(2)	0	0
Rb(2)	41(2)	41(2)	57(2)	20(1)	0	0
I(1)	58(2)	34(2)	59(2)	17(1)	-12(1)	-24(2)
Cl(1)	58(2)	34(2)	59(2)	17(1)	-12(1)	-24(2)
I(2)	101(5)	42(4)	64(4)	21(2)	-22(2)	-43(3)
Cl(2)	101(5)	42(4)	64(4)	21(2)	-22(2)	-43(3)

The anisotropic displacement factor exponent takes the form: $-2\pi^2[h^2a^{*2}U_{11} + ... + 2hka^*b^*U_{12}]$.

Table S9. Bond lengths [Å] for $Rb_3Bi_2I_5Cl_4$ at 293 K with estimated standard deviations in parentheses.

Label	Distances
Bi-I(1)	2.909(3)
Bi-Cl(1)	2.909(3)
Bi-I(2)	3.0546(12)
Bi-Cl(2)	3.0546(12)
Rb(1)-I(1)	4.188(3)
Rb(1)-I(2)	4.1837(9)
Rb(2)-I(1)	4.187(2)
Rb(2)-I(2)	4.073(4)

Table S10. Selected bond angles [°] for $Rb_3Bi_2I_5Cl_4$ at 293 K with estimated standard deviations in parentheses.

Label	Angles
I(1)-Bi-I(1)	93.51(8)
I(1)-Bi-Cl(2)	89.91(4)
Cl(2)-Bi-Cl(2)	86.44(4)

References

1. McCall, K. M.; Liu, Z.; Trimarchi, G.; Stoumpos, C. C.; Lin, W.; He, Y.; Hadar, I.; Kanatzidis, M. G.; Wessels, B. W., α-Particle Detection and Charge Transport Characteristics in the $A_3M_2I_9$ Defect Perovskites (A = Cs, Rb; M = Bi, Sb). *ACS Photonics* **2018,** *5* (9), 3748-3762.
2. McCall, K. M.; Stoumpos, C. C.; Kostina, S. S.; Kanatzidis, M. G.; Wessels, B. W., Strong Electron–Phonon Coupling and Self-Trapped Excitons in the Defect Halide Perovskites $A_3M_2I_9$ (A = Cs, Rb; M = Bi, Sb). *Chem. Mater.* **2017,** *29* (9), 4129-4145.
3. Grushka, E., Characterization of exponentially modified Gaussian peaks in chromatography. *Anal. Chem.* **1972,** *44* (11), 1733-1738.
4. Pezzoli, F.; Qing, L.; Giorgioni, A.; Isella, G.; Grilli, E.; Guzzi, M.; Dery, H., Spin and energy relaxation in germanium studied by spin-polarized direct-gap photoluminescence. *Phys. Rev. B* **2013,** *88* (4), 045204.
5. Pelant, I.; Valenta, J., *Luminescence Spectroscopy of Semiconductors*. Oxford University Press: New York, 2012.
6. Schmidt, T.; Lischka, K.; Zulehner, W., Excitation-power dependence of the near-band-edge photoluminescence of semiconductors. *Phys. Rev. B* **1992,** *45* (16), 8989-8994.
7. Toyozawa, Y., Further Contribution to the Theory of the Line-Shape of the Exciton Absorption Band. *Prog. Theor. Phys.* **1962,** *27* (1), 89-104.
8. Rudin, S.; Reinecke, T. L.; Segall, B., Temperature-dependent exciton linewidths in semiconductors. *Phys. Rev. B* **1990,** *42* (17), 11218-11231.
9. Stadler, W.; Hofmann, D. M.; Alt, H. C.; Muschik, T.; Meyer, B. K.; Weigel, E.; Müller-Vogt, G.; Salk, M.; Rupp, E.; Benz, K. W., Optical investigations of defects in $Cd_{1-x}Zn_xTe$. *Phys. Rev. B* **1995,** *51* (16), 10619-10630.
10. Dawson, R. K.; Pooley, D., F Band Absorption in Alkali Halides as a Function of Temperature. *Phys. Status Solidi B* **1969,** *35* (1), 95-105.
11. Luo, J.; Wang, X.; Li, S.; Liu, J.; Guo, Y.; Niu, G.; Yao, L.; Fu, Y.; Gao, L.; Dong, Q.; Zhao, C.; Leng, M.; Ma, F.; Liang, W.; Wang, L.; Jin, S.; Han, J.; Zhang, L.; Etheridge, J.; Wang, J.; Yan, Y.; Sargent, E. H.; Tang, J., Efficient and stable emission of warm-white light from lead-free halide double perovskites. *Nature* **2018,** *563* (7732), 541-545.
12. Wright, A. D.; Verdi, C.; Milot, R. L.; Eperon, G. E.; Perez-Osorio, M. A.; Snaith, H. J.; Giustino, F.; Johnston, M. B.; Herz, L. M., Electron-phonon coupling in hybrid lead halide perovskites. *Nat. Commun.* **2016,** *7*, 11755.
13. Pankove, J. I., *Optical Processes in Semiconductors*. Dover: New York, 1971.